High damage-resistance and fracture toughness of transparent Nb-doped barium aluminoborate glass ceramics

Zhang, Qi; Sun, Daming; Du, Tao; Jensen, Lars Rosgaard; Wang, Deyong; Popok, Vladimir; Youngman, Randall E.; Smedskjær, Morten Mattrup

Published in:
Applied Materials Today

DOI (link to publication from Publisher):
10.1016/j.apmt.2023.101888

Publication date:
2023

Document Version
Publisher's PDF, also known as Version of record

Applied Materials Today 34 (2023) 101888

Contents lists available at ScienceDirect

Applied Materials Today

journal homepage: www.elsevier.com/locate/apmt

High damage-resistance and fracture toughness of transparent Nb-doped barium aluminoborate glass ceramics

Qi Zhang [a], Daming Sun [a], Tao Du [a], Lars R. Jensen [b], Deyong Wang [b], Vladimir Popok [b], Randall E. Youngman [c], Morten M. Smedskjaer [a,*]

[a] Department of Chemistry and Bioscience, Aalborg University, Aalborg, Denmark
[b] Department of Materials and Production, Aalborg University, Aalborg, Denmark
[c] Science and Technology Division, Corning Incorporated, Corning, NY, USA

ARTICLE INFO

Keywords:
Glass ceramics
Toughening
Microstructure
Piezoelectric crystals
Fracture toughness

ABSTRACT

Glass-ceramics offer the opportunity to address the main disadvantage of oxide glasses, namely low fracture toughness. The presence of crystals can improve the fracture toughness (crack growth resistance), but the crack initiation resistance will typically be deteriorated due to the induced residual stresses. Excessive crystal content and large crystal size can also lead to a loss of transparency. In this work, we report a Nb-doped barium aluminoborate glass-ceramic, for which both the crack initiation resistance (*CR*) and fracture toughness (K_{Ic}) get improved upon heat treatment, while still maintaining some transparency. Relying on combined structural and mechanical characterizations, we demonstrate that the coordination numbers of B and Al in the glass phase decrease upon heat treatment, which is beneficial to energy dissipation under mechanical stress to improve *CR*. Furthermore, the formed piezoelectric crystal phase $BaNb_2O_6$ also helps to improve both *CR* and K_{Ic}, likely by converting the stress-induced mechanical energy into electric energy. Meanwhile, the increase in crystallinity and crystal size after heat treatment also leads to higher K_{Ic} of the glass-ceramics. These findings thus help address the difficult problem of simultaneously improving the resistances to crack initiation and growth, which will facilitate the future design of transparent, yet highly damage-resistant and damage-tolerant glass ceramics.

1. Introduction

Oxide glass materials are widely used in energy, medicine, electronics and advanced communication devices, due to the unique characteristics of glass such as formability, transparency, hardness, and relatively low cost [1,2]. However, these materials lack a stable shearing mechanism, and thus exhibit low fracture toughness (K_{Ic}). While the crack initiation resistance (*CR*) can be improved through composition optimization and/or post-processing, it is challenging to simultaneously improve K_{Ic} and *CR*. For example, Januchta et al. discovered an oxide glass with ultra-high *CR* by optimizing the glass composition using adaptive networks [3], but the fracture toughness of this as well as other commercially available homogeneous oxide glasses remains to be below 1 MPa·m$^{0.5}$ [4,5]. To obtain high fracture toughness, researchers have found that when crystals are introduced into the glass matrix, K_{Ic} can be effectively improved by increasing the crack path length to dissipate the mechanical energy [6,7]. Hence, the so-called glass-ceramics made from partial crystallization of glasses have attracted significant attention for their potential in fabricating high-K_{Ic} materials.

Glass-ceramics can be prepared through heat treatment of a precursor glass, as the thermal energy allows for nucleation and growth of crystals in a glassy matrix [8]. Glass-ceramics with high crystal volume fraction, large crystal size, and large aspect ratio of crystals generally exhibit higher fracture toughness [9–11]. For example, Beall et al. have fabricated glass-ceramics with fracture toughness in the range of 3.5 to 4.6 MPa·m$^{0.5}$ [12], which are more than five times higher than that of soda lime silica (window) glass. However, two other important properties, crack initiation resistance and transparency, are also influenced by the crystals in the glass matrix. Residual stress is the driving force for crack initiation [13], and crystalline phase transformations as well as the thermal expansion coefficient mismatch between glass and crystal during heat treatment can introduce stresses into the glass matrix [6,10]. This can lead to a decreased resistance to crack initiation [6]. In addition, the transmittance of the glass-ceramics tends to decrease as the fraction or size of the crystals increases [14,15] as well when the mismatch in refractive index of the glass and crystalline phases

* Corresponding author.
E-mail address: mos@bio.aau.dk (M.M. Smedskjaer).

https://doi.org/10.1016/j.apmt.2023.101888
Received 20 March 2023; Received in revised form 27 June 2023; Accepted 27 July 2023
Available online 4 August 2023

increases. That is, although large crystals in glass matrix seem to be more effective in improving the fracture toughness of glass-ceramics, they will lead to a decrease in transmittance (unless the refractive indices of crystal and glass phases can be well matched) and also lower the crack initiation resistance according to the previous studies. Furthermore, the glass network structure also changes during the heat treatment (except in the case of congruent crystallization) [16,17], which also affects the mechanical properties of the glass-ceramics. In the case of homogeneous glasses, there is no direct relationship between the crack initiation resistance and fracture toughness [18], and it is thus challenging to improve the crack resistance and fracture toughness simultaneously while also maintaining high transmittance in glass-ceramics. New strategies are thus needed beyond modifying the heat treatment conditions to control the type, content and size of crystals in glass-ceramics.

Energy dissipating processes can occur through different structural rearrangements. Oxide glasses containing self-adaptive network constituents, such as B_2O_3 or Al_2O_3, can exhibit good crack resistance since the coordination number of these network-forming species can increase even at modest stresses (such as those during sharp contact loading) to dissipate energy [3]. Therefore, in this work, we choose an aluminoborate composition as a base glass system to facilitate such structural transition. Then, to further enhance such structural transitions that can dissipate mechanical energy, we propose to embed a piezoelectric crystal phase in this adaptive glass matrix. Research on piezoelectric composite ceramics has shown that the toughness can be enhanced through the incorporation of a piezoelectric secondary phase in the matrix [19] and we expect that a similar effect can be found in glass-ceramics. In the case of an aluminoborate matrix, we therefore here added BaO and Nb_2O_5 to the base composition to obtain a Nb-containing piezoelectric crystal second phase in the glass matrix upon heat treatment. Previously, a borosilicate glass-ceramic with Nb-containing needle-shaped crystal phase for sealing applications has shown good thermo-mechanical cycling stability [20]. Results reported by Dong et al. indicate that the formation of a $Ba_3Nb_{10}O_{28}$ crystalline phase can enhanced the crack resistance, but no detailed crack resistance data were reported [21]. In addition, Gallo et al. have reported a transparent MgO-Al_2O_3-SiO_2 glass-ceramic with improved fracture toughness and hardness after crystallization [22]. That is, by tuning the crystallization process, it is possible to achieve improved mechanical properties while maintaining the transparency. However, none of the above reported glass-ceramics have achieved simultaneous improvement in fracture toughness and crack resistance while maintaining a large degree of transparency. Here, we present a new approach based on a piezoelectric phase in a structurally adaptive matrix to achieve the unusual combination of transparency and improved K_{Ic} and CR .

2. Methods

2.1. Sample preparation

We synthesized the glass of composition 23BaO-18.4Al_2O_3-50.6B_2O_3-8Nb_2O_5 (in mol%) by melting a homogeneous mixture of reagent grade materials ($BaCO_3$, H_3BO_3, Al_2O_3 and Nb_2O_5) in PtRh crucible at 1300 °C for 2 h. Then the melt was quenched by pouring it onto a copper plate to obtain a glass material. To improve the homogeneity of the glass and thus the subsequent crystallization, we remelted the crushed glass pieces at 1300 °C for another 2 h. Finally, this melt was quenched onto the stainless-steel plate to obtain a glass. This bulk glass sample was quickly moved to a preheated annealing furnace at an estimated glass transition temperature (T_g) value of 580 °C (based on the previous studies [23]) for 30 min and cooled down to room temperature. A small piece of glass was cut from the annealed bulk glass and then used to measure the actual T_g value (see Section 2.3). The glass was re-annealed at the measured T_g. This as-prepared annealed glass was named BN0. In order to easily control the crystallization process and obtain transparent samples with varying crystal content and size, we choose 600 °C as the heat-treatment temperature (slightly higher than T_g) for different heat treatment durations. We note that the glass-ceramics undergo bulk homogeneous crystallization. Some pieces of glass were cut from the annealed bulk glass and subjected to heat treatment at 600 °C for 4, 8, 12, and 16 h. These samples were named BN4, BN8, BN12 and BN16, respectively (Table 1). The specimens for glass structure and properties testing were polished in ethanol (to avoid any surface corrosion) using SiC paper with decreasing abrasive particle size (up to grit 4000), followed by polishing in a water-free 1 μm diamond suspension.

2.2. Structural characterization

The crystalline phase and changes in crystal content in the glass-ceramic samples were identified by X-ray diffraction (XRD, Empyrean XRD, PANalytical) analysis using a monochromator Cu Kα radiation (1.5406 Å). The spectra were recorded in the range of 10°-70° at 40 kV with a scanning speed of 8° min^{-1}. The tested specimens were well-polished as-prepared and heat-treated bulk samples. The polished surfaces were also used to test structure and other properties as explained in the following. The crystalline content (wt. %) in the glass-ceramics was calculated from the XRD results using the peak function of Jade software [24].

The morphology of the crystal phase in the glass-ceramics was investigated using a field emission scanning electron microscopy (SEM) (Zeiss 1540 XB) at an acceleration voltage of 10 kV. These measurements were performed on etched samples to improve the contrast. The polished specimens were etched using 1 wt.% HF for 10 s and then coated with gold. For the BN16 sample, we also investigated the path of a crack induced by indentation and in this case, the sample was not etched. All samples were gold coated before testing. The size distribution of the crystal phase was analyzed based on the SEM images using the ImageJ software [25,26].

Solid-state nuclear magnetic resonance (NMR) spectroscopy measurements were performed to investigate the changes in the short-range order structure around the NMR-active nuclei ^{11}B, ^{27}Al and ^{93}Nb upon heat treatment. ^{11}B and ^{27}Al magic-angle spinning (MAS) NMR spectra were acquired on an Agilent DD2 spectrometer with a 3.2 mm MAS NMR probe at a magnetic field of 16.4 T. Powdered glass samples were packed into 3.2 mm outer diameter zirconia rotors and spun at 20 and 22 kHz for ^{11}B and ^{27}Al MAS NMR, respectively. The data were collected at resonance frequencies of 224.5 and 182.3 MHz for ^{11}B and ^{27}Al, respectively, while a short radiofrequency (rf) pulse of 0.6 μs (π/12 tip angle) was used with a recycle delay of 5 s and 2 s for ^{11}B and ^{27}Al, respectively. Signal averaging was performed using 600 to 1000 scans for each sample. All NMR data were processed without any additional line broadening. The data were plotted using the normal shielding convention, while the frequency of ^{11}B and ^{27}Al data were referenced to aqueous boric acid (19.6 ppm) and aqueous aluminum nitrate (0.0 ppm), respectively. The DMFit software was used to fit the ^{11}B and ^{27}Al MAS NMR data [27]. Multiple second-order quadrupolar lineshapes, described using the "Q mas ½" function, were used to fit the three-fold coordinated boron resonances, while fitting of the four-fold

Table 1
Nominal chemical compositions and properties of the glass and glass-ceramic samples, including glass transition temperature (T_g), density (ρ), Young's modulus (E), and Poisson's ratio (ν). The errors in T_g, ρ, E, and ν do not exceed ± 3°C, 0.001 g/cm^3, 0.1 GPa, and 0.001, respectively.

Sample ID	Heat treatment	T_g (°C)	Density (g/cm^3)	Young's modulus (GPa)	Poisson's ratio
BN0	-	575	3.307	66.0	0.286
BN4	600 °C 4 h	573	3.297	65.2	0.287
BN8	600 °C 8 h	572	3.295	65.0	0.287
BN12	600 °C 12 h	572	3.290	65.5	0.286
BN16	600 °C 16 h	573	3.284	66.1	0.282

coordinated boron peak was accomplished with a mixed Gaussian/-Lorentzian peak. A small overlapping satellite transition spinning sideband (see supplemental Fig. S1) from four-fold coordinated boron was estimated from the shape and position of the first set of spinning sidebands at approximately +90 and -88 ppm, and this extra intensity was not included in determination of the fraction of four-fold coordinated boron (N_4). The CzSimple lineshape model was used for ^{27}Al, and provides an accurate representation of these lineshapes and distributions in their quadrupolar coupling constants and isotropic chemical shifts. All fitting results for ^{11}B and ^{27}Al MAS NMR spectra are given in supplement Table 1.

^{93}Nb MAS NMR spectra were obtained at 16.4 T (171.04 MHz) using a solid-echo pulse sequence consisting of 1 and 2 μs radio-frequency pulse widths and whole echo acquisition enabled by a 100 μs delay between the two pulses. Signal averaging involved 25000 to 61000 transients with a recycle delay of 1 s. Samples were powdered and loaded into 3.2 mm zirconia rotors with sample spinning at 20.0 kHz. ^{93}Nb MAS NMR data were processed by shifting the time domain signal to the echo maximum, followed by Fourier transforming and phasing the resulting spectra. 200 Hz line broadening was utilized, and the data were frequency referenced using the International Union of Pure and Applied Chemistry (IUPAC) method of ratioing the shift of ^{93}Nb relative to that measured with another nucleus (i.e., ^{11}B in 0.1M boric acid solution at 19.6 ppm) [28,29].

Micro-Raman spectroscopy (inVia, Renishaw) measurements were performed to obtain further structural information at the medium-range length scale. The Raman spectra were acquired on surfaces of polished samples in the 120-1600 cm^{-1} wavenumber range. To confirm the homogeneity of the sample surfaces, spectra were collected from five different surface locations. Measurements were done using a 532 nm diode pumped solid state laser for an acquisition time of 10 s, and all spectra were uniformly treated in Origin software for background correction and area normalization.

2.3. Property characterization

The optical transparency of the as-prepared glass and heat-treated glass-ceramic samples was determined using ultraviolet-visible (UV-VIS) spectroscopy (Cary 50 Bio, Varian). The polished samples with ~1.5 mm thickness were used for the tests, and the spectra were acquired in the 200-800 nm wavelength range. All the presented UV-VIS transmittance spectra were normalized to a thickness of 1 mm.

The glass transition temperature (T_g) of the as-prepared glass and heat-treated glass-ceramic samples were measured using differential scanning calorimetry (DSC) (STA 449 F1, Netzsch). The tested samples were polished down to 1 mm thick. Each sample was placed in a Pt crucible under a flow of argon (gas flow 40 mL·min^{-1}). The heating rate was 10 K·min^{-1}, and after reaching the maximum temperature of 700 °C, the sample was cooled down to room temperature at a rate of 20 K·min^{-1}. The intercept between the tangent to the inflection point of the endothermic peak and the extrapolated heat flow of the glass was taken as the T_g. The error in the determined T_g value is around ± 3 °C.

We used Archimedes' principle of buoyancy to determine the density (ρ) of all samples. The samples (around 1.5 g in mass) were tested ten times in both air and ethanol, and the density value was the average of these measurements. The elastic properties of the samples were measured by ultrasonic echography using an ultrasonic thickness gauge (38DL Plus, Olympus) equipped with 20 MHz delay line transducers. Then, Young's modulus (E) as well as Poisson ratio (υ) were calculated using the relationships for isotropic materials [30].

The coefficient of thermal expansion (CTE) of the as-prepared glass was measured by dilatometry (DIL402C, Netzsch) at a heating rate of 2 °C min^{-1} in air. It was taken as the slope of the expansion curve in the temperature range from 200 to 500 °C.

Vickers hardness (H_V), crack initiation resistance (CR), and indentation fracture toughness (K_{Ic}^{IFT}) of the samples were determined by using a Nanovea CB500 hardness tester. A Vickers indenter tip (four-sided pyramid-shaped diamond with an angle of 136°) was used for the hardness and crack resistance measurements, while a sharper 100° indenter tip (with the same pyramid geometry) was used for the indentation fracture toughness measurements. All indentations experiments were conducted under ambient conditions, with a temperature of ~295 K and a relative humidity of 29 ± 4%.

The hardness (H_V) values were calculated as $H_V = 1.8544P/d^2$, where P is the contact load and d is the average length of the indent diagonals. Twenty indents were performed for each specimen at a load of 3 N applied for 10 s and the reported H_V value is the average of these 20 indents. Crack resistance (CR) is typically defined as the resistance of the material towards corner crack initiation upon Vickers indentation. Following the method of Wada [31], the probability of crack initiation is defined as the ratio between the number of cracked corners and the total number of corners on all indents. CR was then determined as the load at which the crack probability is 50%. Each polished glass specimen was indented 30 times at different loads (from 0.49 N to 30 N) with a loading duration of 15 s and a dwell time of 10 s. The loading rate was 9.8 N/min. Then the number of cracked corners was counted at each load to determine CR from the crack probability vs. load curve.

To evaluate the indentation deformation mechanism of the glasses and glass-ceramics, we determined the recovery of the indent side length. Ten indents were performed on the polished sample surface at a load of 3 N with a loading duration of 15 s and a dwell time of 10 s. The indentation side length ($L_{s,i}$) was measured using the optical microscope. Then the indented samples were annealed at 0.9T_g (scaled in Kelvin) for 2 h, and the indentation side length after annealing ($L_{s,f}$) was measured again. The contribution of densification to the indentation deformation was then estimated from the annealing-induced side length recovery (L_{SR}) using $L_{SR} = \frac{L_{s,i} - L_{s,f}}{L_{s,i}}$ [30,32,33]. It is important to note that this method is developed for glass materials and the heat-treatment likely only provides the glass matrix with the ability to recover its densified volume during the 0.9T_g annealing. We also note that the T_g did not change significantly upon crystallization (Table 1), i.e., the annealing temperature did not vary significantly.

Fracture toughness describes the material's resistance to crack growth, and here we used two methods to evaluate it. While the indentation fracture toughness is a widely used method to measure fracture toughness because of the ease of use and small specimen sizes, it is not as reliable as self-consistent methods such as single-edge pre-crack beam (SEPB). Here, we test and compare the results from both methods. First, indentation fracture toughness (K_{Ic}^{IFT}) was determined using the indentation method and calculated based on crack length measurements. To avoid or limit the effect of densification on K_{Ic}^{IFT} during indentation, we used a sharper 100° indenter tip for the indentation based on the work of Gross et al. [34]. K_{Ic}^{IFT} was then determined using the equation from Anstis et al. [35],

$$K_{IFT} = \xi \left(\frac{E}{H}\right)^{0.5} \left(\frac{P}{C_0^{\,1.5}}\right) \quad (1)$$

where ξ is an empirically determined constant for an indenter that was calibrated against select material, here ξ is set as 0.035 [36]. E is Young's modulus, P is the indentation load, H is the hardness at the load P using the 100° indenter tip, and c_0 is the average length of the radial/median cracks measured from the center of the indent impression. The indentation image was captured immediately after the test and then was used to measure the crack length. Ten indents were generated for each polished specimen at 0.98 N with a loading duration of 15 s and a dwell time of 10 s. The loading rate was 9.8 N/min. The reported K_{Ic}^{IFT} value is the average of these ten indentation results.

Second, we also used the single-edge pre-crack beam (SEPB) method to evaluate the fracture toughness (K_{Ic}^{SEPB}) of the glasses and glass-ceramics following the well-established procedure [37,38]. Five polished beams with dimensions of about 1.5×2×10 mm^3 were prepared

for all samples. Eight Vickers indents with a load of 9.8 N for a dwell time of 5 s were then placed on a line on the breadth side ($B = 1.5$ mm). The indented specimen was placed in a bridge-compressive fixture with a groove size of approximately 3 mm (1.5 times the specimen width, $W = 2$ mm) to produce a pre-crack with a cross-head speed of 0.05 mm·min^{-1}. A crack was initiated from the indent corners, and then propagated until it reached the middle of the specimen width. Afterwards, the pre-cracked specimen was positioned in a three-point bending fixture and the specimen was fractured with a cross-head speed of 10 μm·s^{-1} to avoid humidity effects [37]. The adapted three-point bending span (S) of about 8 mm was designed to fulfill the span-to-width ratio of at least ~4 to avoid the span-length dependence. K_{Ic}^{SEPB} was then calculated from the peak load (P_{max}),

$$K_{Ic} = \frac{P\max}{B\sqrt{W}}\, Y\, *, \text{ where } Y* = \frac{3}{2}\frac{S}{W}\frac{\alpha^{1/2}}{(1-\alpha)^{3/2}} f\,(\alpha) \tag{2}$$

where α is the pre-crack-width ratio (a/W) and $f(\alpha) = [1.99 - (\alpha - \alpha^2)(2.15 - 3.93\alpha + 2.7\alpha^2)]/(1 + 2\alpha)$. The average K_{Ic}^{SEPB} value was calculated from the results of five valid tests. More details on the methods can be found elsewhere [37,38].

2.4. Density functional perturbation calculations

We investigated the piezoelectric properties of the formed crystal phase ($BaNb_2O_6$) based on density functional perturbation theory (DFPT) calculations. This was done using the Vienna Ab-initio simulation package (VASP) [39,40] with plane wave basis sets and the projector augmented-wave (PAW) method. Exchange-correlation effects were treated using the Perdew-Burke-Ernzerhof (PBE) implementation of the generalized gradient approximation (GGA) [41]. The Brillouin zone integration was obtained by an 8×6×3 Monkhorst–Pack k-points grid and the energy cutoff was set to 550 eV. The criterion for energy convergence was set as 10^{-6} eV.

3. Results and discussion

3.1. Phase microstructure analysis

Fig. 1a shows the XRD patterns of the as-prepared glass and glass-ceramic samples. To further confirm the identity of the crystal phase, the XRD pattern of a sample heat-treated at 600 °C for 48 h and $BaNb_2O_6$ standard card are shown in Fig. 1b. As shown in Fig. 1a, the as-prepared glass and glass-ceramics held at 600 °C for 4 h are X-ray amorphous, as no sharp diffraction peaks are observed in the BN0 and BN4 samples. As the duration of heat treatment is extended to 8 h, a small peak appears at $2\theta = 23°$. As the heat treatment time is further extended to 16 h, more sharp peaks appear and their intensities increase due to evolving crystallinity. Based on the results in Fig. 1, we identify only one type of crystal in the glass-ceramics, namely the piezoelectric $BaNb_2O_6$ phase (ICDD Card No. 32-0077). According to the analysis of the XRD results, we roughly estimate the crystallinity of the BN8, BN12 and BN16 samples to bee < 1%, 5% and 10% (in wt.%), respectively.

Fig. 2 shows the SEM crystal morphology in the samples heat-treated at 600 °C for 8, 12 and 16 h. There are no obvious crystals observed in the as-prepared and 4 h heat-treated samples. The grey region is dominant in the glass-ceramics, whereas some white regions are distributed in the grey region. Considering that only one type of crystal ($BaNb_2O_6$) is present in the samples according to the XRD results, we can assign the white region to this crystal phase, while the grey regions represent the residual glass matrix phase. The crystals are found to be distributed homogeneously throughout the glass matrix in all samples. As the heat treatment time increases, the average crystal size (based on image analysis) increases from ~15 nm in BN8 to ~30 nm in BN12, although we note that there are still some small-sized crystals in BN12. When the heat treatment time is extended to 16 h, the average crystal size increases to ~50 nm. Hence, both the amount and size of the crystals increase upon heat treatment. Based on the XRD and SEM results, we thus conclude that with the prolongation of heat-treatment time at 600 °C, both the content and size of $BaNb_2O_6$ crystals increase.

Next, we have performed DFPT calculations to investigate the piezoelectric properties of the $BaNb_2O_6$ crystals. This DFPT method has previously been applied in calculating the piezoelectricity of various systems such as $BaTiO_3$ [42] and meta-nitroaniline [43]. The piezoelectric stress coefficients e_{ij} can be obtained as:

$$e_{ij} = \frac{\partial P_i}{\partial \varepsilon_j} \tag{3}$$

where P_i is the polarization in the direction i and ε_j is applied stress in the direction j. The lattice parameters of the $BaNb_2O_6$ crystal after structural optimization (Supporting Fig. S1) are $a = 3.9321$ Å, $b = 6.1708$ Å, and $c = 10.6171$ Å. The maximum absolute value of the piezoelectric stress coefficient e_{ij} tensor component is then found to be 0.88 C/m^2. A threshold value of 0.5 C/m^2 for piezoelectricity has previously been proposed in Ref. [44]. Therefore, these calculations confirm that the $BaNb_2O_6$ crystal exhibits good piezoelectricity.

3.2. Glass-ceramics network structure

Since the heat-treatment process both results in the precipitation of crystals as well as changes of the glass structure, we analyze both the glass and glass-ceramic samples using NMR and Raman spectroscopy in the following. Fig. 3 shows the ^{11}B, ^{27}Al and ^{93}Nb MAS NMR spectra, where the spectra of Fig. 3a and b are normalized by the intensity of the strongest peak. The deconvolution results, the average coordination number of aluminum, and N_4 (the fraction of tetrahedral to total boron)

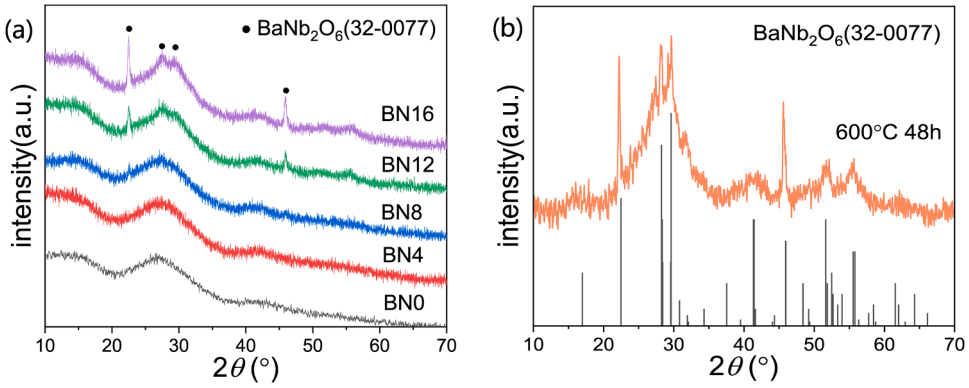

Fig. 1. XRD patterns of (a) as-prepared glass and glass-ceramic samples heat-treated at 600°C for 4 to 16 h and (b) glass-ceramic sample after heat treatment at 600°C for 48 h. The $BaNb_2O_6$ standard spectrum is also shown in panel (b).

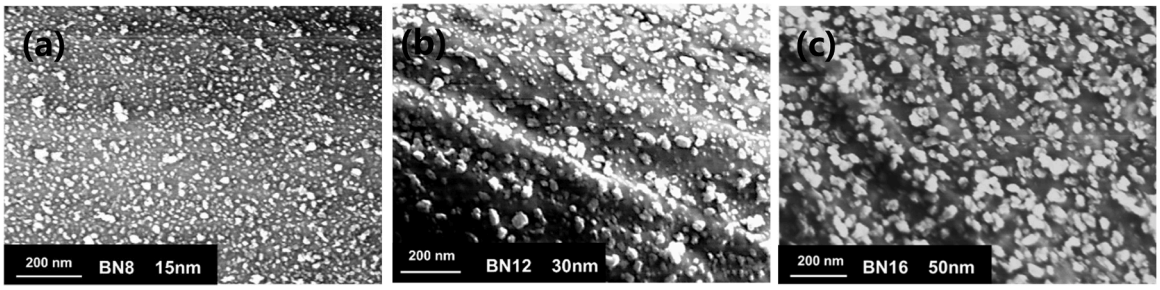

Fig. 2. SEM morphology of the etched heat-treated glass-ceramics samples using InLens detector: (a) BN8, (b) BN12, and (c) BN16.

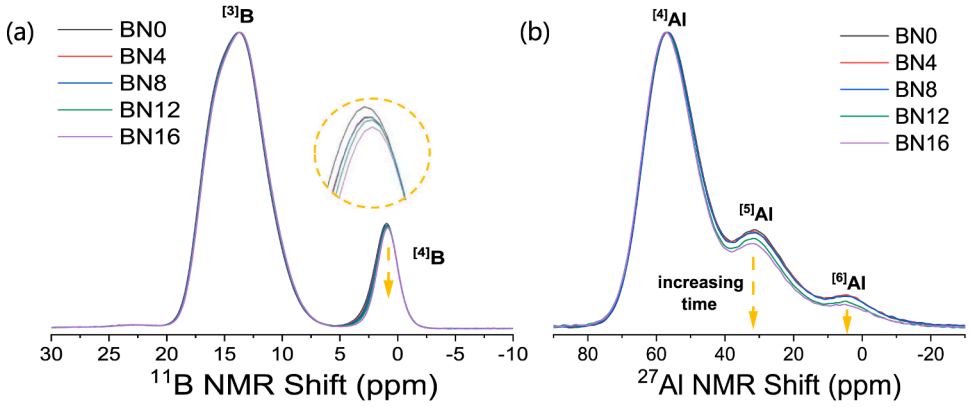

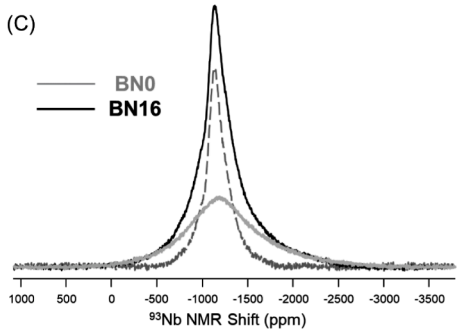

Fig. 3. MAS NMR spectra of the as-prepared glass and glass-ceramic samples: (a) ^{11}B, (b) ^{27}Al and (c) ^{93}Nb. The inset in (a) is an expanded view of the $^{[4]}$B peak maxima, showing a subtle decrease in intensity with heat treatment time. ^{93}Nb MAS NMR spectra scaled to approximately the same intensity of broad signal from Nb in glassy environments. The spectral subtraction (dashed line) shows a crude estimate on the extent of Nb partitioning into the niobate crystal phase (45 atom% in this example).

are summarized in Table 2. The full tabulation of ^{11}B and ^{27}Al MAS NMR fitting results is given in Supporting Table S1 and Table S2. The normalized ^{11}B MAS NMR spectra are shown in Fig. 3a. The peak centered near -1 ppm is assigned to $^{[4]}$B, while the broad peak located at 5~20 ppm can be assigned to $^{[3]}$B units [45]. The intensity of the peak associated with $^{[4]}$B decreases relative to that of $^{[3]}$B upon heat treatment. Based on the deconvolution, we thus find that N_4 decreases from 12.1% in the as-prepared glass to 10.4% in the 16 h heat-treated sample, i.e., the crystallization process promotes a partial $^{[4]}$B to $^{[3]}$B transition. The deconvoluted spectra are shown in Supporting Fig. S2.

Table 2
Boron and aluminum speciation as determined from deconvolution of the ^{11}B and ^{27}Al MAS NMR spectra. The uncertainty in the area fraction is 0.2%, while the uncertainty in N_4 and average coordination number of aluminum is on the order of ± 0.2% and ± 0.01, respectively.

Sample ID	B sites		N_4 (%)	Al sites			Average Al CN
	$^{[3]}$B Area (%)	$^{[4]}$B Area (%)		$^{[4]}$Al Area (%)	$^{[5]}$Al Area (%)	$^{[6]}$Al Area (%)	
BN0	87.9	12.1	12.1	75.3	20.3	4.4	4.29
BN4	88.4	11.6	11.6	75.4	20.3	4.3	4.29
BN6	88.7	11.3	11.3	75.3	20.2	4.5	4.30
BN12	89.1	10.9	10.9	77.0	19.3	3.7	4.27
BN16	89.6	10.4	10.4	78.0	18.4	3.6	4.26

The ^{27}Al MAS NMR spectra can be deconvoluted into three Al resonances, centered around ~63, ~36, and ~9 ppm and corresponding to $^{[4]}$Al, $^{[5]}$Al, and $^{[6]}$Al, respectively. The deconvoluted spectra are shown in Supporting Fig. S3. As observed in Fig. 3b, the intensities of the peaks associated with $^{[5]}$Al and $^{[6]}$Al decrease upon heat treatment compared to the as-prepared glass. The fraction of $^{[4]}$Al increases from 75.3% in BN0 to 78.0% in the BN16 sample, while the fractions of $^{[5]}$Al and $^{[6]}$Al decrease from 20.3% and 4.4% in BN0 to 18.5% and 3.6% in BN16, respectively. In conclusion, the average coordination number of aluminum decreased from 4.29 for the as-prepared glass to 4.26 for the 16 h heat-treated sample, i.e., the $^{[5]}$Al and $^{[6]}$Al structures partially transform to $^{[4]}$Al upon crystallization of the $BaNb_2O_6$ phase. These NMR results also confirm that crystallization as a result of heat-treatment of this particular glass composition does not appear to

result in Al- or B-containing phases. That is, all spectra in Fig. 3a and b are consistent with B and Al remaining in the residual glass.

Fig. 3c shows the ^{93}Nb NMR spectra. The broad band in the BN0 sample located in the range of -900 to -1300 ppm can be attributed to niobium in six-fold coordination, indicating that niobium plays the role of a network modifier [46,47]. After heat treatment at 600 °C for 16 h, the MAS NMR shift of the band moves from -1225 ppm in the as-prepared glass to -1163 ppm in the BN16 samples and the band also becomes sharper. In Nb-containing bronze-like perovskites for which corner- or edge-sharing occurs exclusively between two Nb polyhedra, the chemical shifts are around -1000 ppm [48]. Therefore, the observed changes upon heat treatment, especially the significant narrowing of the ^{93}Nb resonance, can be ascribed to the $BaNb_2O_6$ crystal formation. If the broad signal from Nb in the glass is subtracted from the ^{93}Nb MAS NMR spectrum of BN16, one can estimate the fraction of Nb partitioning into the crystal phase and also that fraction of Nb remaining in the residual glass. The continued increase in $BaNb_2O_6$ crystal content with prolonged heating, as shown by the XRD results in Fig. 1b, indicate that at lower times, the crystallization process is incomplete. With the simple treatment of ^{93}Nb MAS NMR data, as in Fig. 3c, the fraction of Nb in crystalline $BaNb_2O_6$ is found to be around 45 atom%.

The Raman spectra of the samples in the frequency range of 200-1500 cm^{-1} are shown in Fig. 4a. First, we note that the band related to Al-O-Al bonding in AlO_4 structural units should be located at ~560 cm^{-1}, but we do not observe significant changes upon heat-treatment in this region. The band at 200-400 cm^{-1} can be assigned for O-Nb-O in NbO_6 octahedra [49], the band at ~673 cm^{-1} is assigned to the Nb-O vibrations of an NbO_6 octahedron corner-linked in a three-dimensional network (NbO_6-3D) [50,51], and the band located at ~886 cm^{-1} corresponds to a short Nb-O bond in an NbO_6 octahedron (NbO_6-isolated) [50,52]. The relative intensity of the band assigned to isolated NbO_6 decreases while that of the bands assigned to O-Nb-O in NbO_6 octahedra increases upon heat treatment. The intensity of the band assigned to Nb-O-Nb in NbO_6-3D corners increases significantly after heat treatment. Previous work suggests that the structure of $BaNb_2O_6$ crystal belongs to the family of tungsten bronze frameworks [53,54], i.e., the changes in the Raman spectra confirm that more $BaNb_2O_6$ crystal (or some similar ordered structural units) form upon heat treatment.

The bands at ~727 and ~800 cm^{-1} can be attributed to B-O-B units present in chain metaborate units and boroxol ring structure, respectively. The minor band at ~1053 cm^{-1} is assigned to B-O-B from $^{[4]}$B structure in diborate units, while the bands ranging from 1100-1600 cm^{-1} correspond to B-O$^-$ present in pyroborate, chain and ring metaborate units [55]. These results agree with the ^{11}B MAS NMR results that show two different BO_3 resonances are needed to fit these spectra (Supporting Fig. S2), one of which has a relatively high quadrupolar asymmetry parameter and signifies NBO on BO_3 (such as

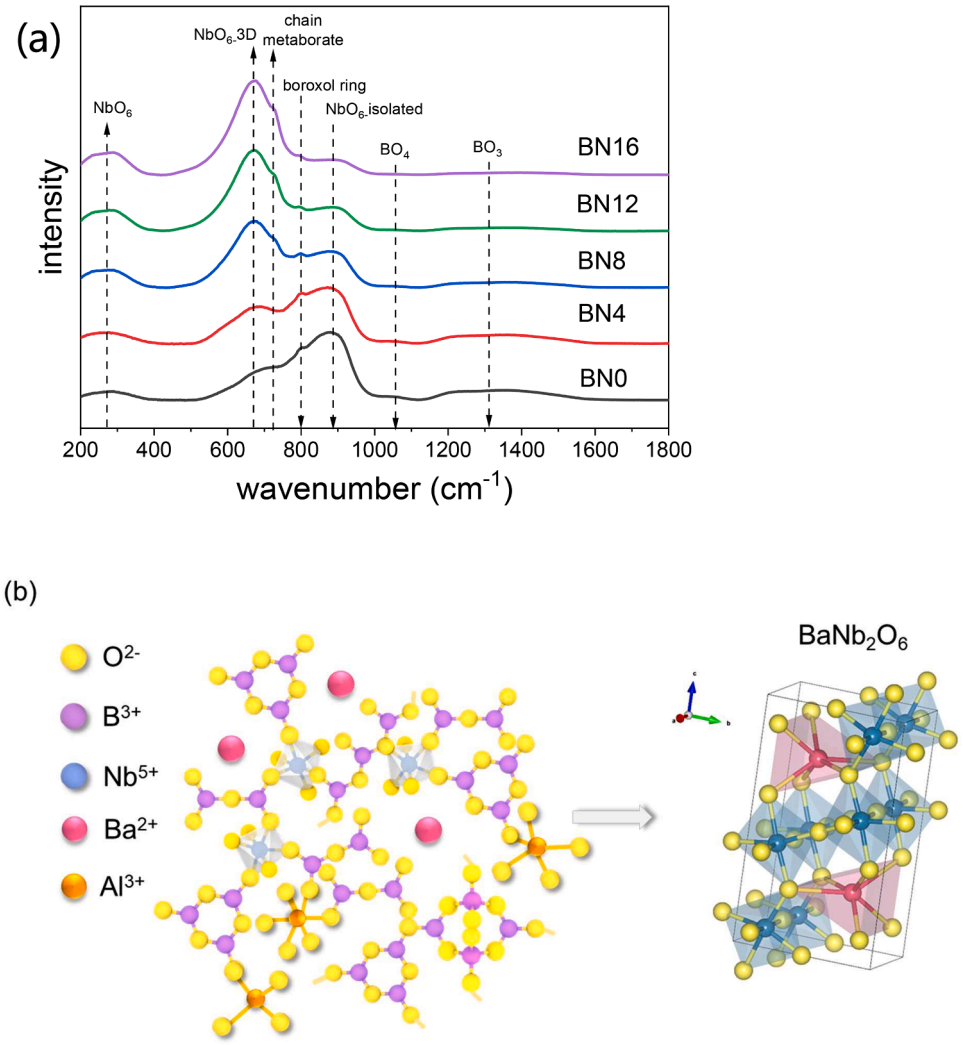

Fig. 4. (a) Raman spectra of the glass and glass-ceramic samples. (b) Structure unit models derived from the NMR and Raman structural characterization. The lefthand side shows the main structure of the as-prepared glass, while the righthand side shows the $BaNb_2O_6$ crystal of tungsten bronze frameworks.

metaborate). After heat treatment, the intensity of the band related to $^{[4]}$B decreases due to the $^{[4]}$B to $^{[3]}$B transition, consistent with the ^{11}B MAS NMR results. In addition, the intensity of the bands related to B-O^{-} (pyroborate, chain and ring metaborate) decreases and the intensity of the band related to B-O-B in chain metaborate units increases, thus indicating that the connectivity of borate network increases upon heat treatment. That is, non-bridging oxygens (B-O^{-}) transform into bridging oxygens (B-O-B) [56]. The decrease in the relative intensity of the band related to boroxol rings implies that borate rings transform into borate chains upon heat treatment. Considering the band assigned to chain metaborate is overlapped by Nb-O band, and combined with the quantitative analysis of NMR results about $^{[3]}$B peak (Supporting Table S1), the B-O network does not change much under the influence of heat treatment and crystallization. This also explains why the T_g of the glasses remain relatively unchanged during the heat treatment. The corresponding structure unit models are shown in Fig. 4b. In the as-prepared glass structure, we find boroxol rings, isolated borate structures (such as pyroborate and ring metaborate) and a smaller amount of diborate units. Nb is mainly present in the form of NbO_6-isolated octahedra, for which the charge is balanced with Ba ions. After heat treatment, the boroxol ring structure transforms to chain metaborates, and $BaNb_2O_6$ crystal of tungsten bronze frameworks or crystal precursors like tungsten bronze frameworks are formed in the glass matrix.

3.3. Glass ceramic properties

Fig. 5a shows photographs of the polished glass and glass-ceramic samples. The BN0 and BN8 samples exhibit good transparency, but as the heat treatment time is prolonged, the samples gradually become translucent. Fig. 5b shows the measured UV-VIS transmittance spectra, confirming the very high transmittance of the BN0 and BN8 samples, which is around 90% in the 400~800 nm wavelength range. However, the transmittance of BN12 and BN16 decreases in this wavelength range (e.g., BN12 has a shoulder at ~400 nm and BN16 has a shoulder at ~500 nm), although the transmittance of BN12 and BN16 is still up to ~90% at a wavelength of 800 nm.

According to the scattering theory, the coefficient of scattering (σ) is governed by the size of crystals (R) dispersed in the glassy phase [$\sigma \propto R^3$], and the refractive index difference between crystal (n) and glass matrix (n_0), $[\sigma \propto \{(n^2 - n_0^2)/(n^2 + n_0^2)\}^2]$ [57]. Sambasiva et al. reported that the refractive index of tungsten bronze structure crystal, such as $Ba_2NaNb_5O_{15}$, is around 2.4 [53], and the refractive index of borate glass is around 1.5 [58].Therefore, the mismatch between the refractive index of crystal and glass cause the glass-ceramics to lose some transmittance with the increase of crystal size and content after heat treatment. Finally, we note that the shoulder peaks in BN12 and BN16 are likely related to the scattering caused by large size crystals in the short wavelength range.

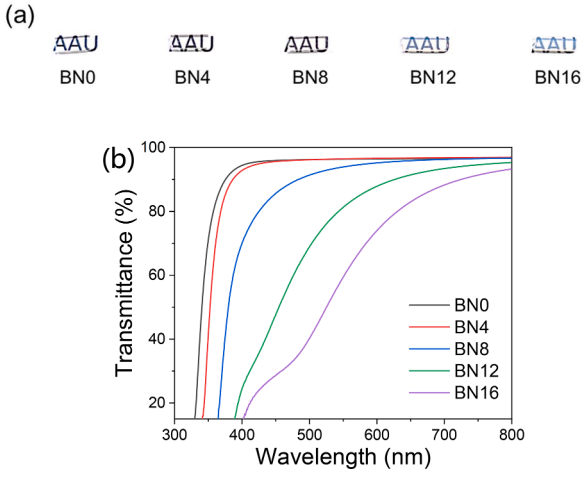

Fig. 5. (a) Photographs of the polished as-prepared glass and glass-ceramics samples with a thickness of 1.5 mm. (b) The UV-VIS transmittance spectra of the as-prepared glass and glass-ceramics samples.

The glass transition temperature, density and elastic properties are summarized in Table 1. These properties generally do not change significantly upon heat treatment. That is, the glass transition temperature for all samples is around 573 K and the density decreases slightly from 3.307 g/cm^3 for BN0 to 3.284 g/cm^3 for BN16. The nearly constant T_g is consistent with the ^{11}B and ^{27}Al NMR data that show very small changes in the residual glass structure upon heat-treatment and $BaNb_2O_6$ crystallization. The Young's modulus and Poisson's ratio for all samples are around 66.0 GPa and 0.28, respectively. Furthermore, the coefficient of thermal expansion of the as-prepared glass is found to be 9.8×10^{-6} °C^{-1}. The corresponding expansion-temperature curve for this sample is shown in Supporting Fig. S4.

The mechanical properties of the glass and glass-ceramic samples are summarized in Table 3, including Vickers hardness (H_V), crack initiation resistance (CR), fracture toughness (K_{Ic}) tested by both indentation and SEPB method, and the crystal average size determined from the SEM images. For the as-prepared glass, the hardness (measured at 3 N load) is about 5.2 GPa, but when the heat treatment time is 16 h at 600 °C, the hardness decreases to 5.1 GPa. Therefore, there is no significant relationship between the hardness and crystallinity of the present glass-ceramics.

Fig. 6a shows the crack initiation probability as a function of applied indentation load, while the determined values of CR are given in Table 3. The crack resistance increases from 5.1 N for as-prepared glass to 9.1 N for BN12, which is the glass-ceramic heat-treated at 600 °C for 12 h. When the heat treatment time is further prolonged to 16 h, the crack resistance of BN16 decreases to around 7.9 N, but still higher than that of BN0, BN4 and BN8. Overall, the crack initiation resistance therefore increases upon crystallization. Densification during the indentation procedure is believed to be beneficial to dissipate energy and thus improve the crack resistance [59]. Thus, the side length (and thus volume) recoveries of the Vickers indent produced at 3 N before and after annealing at 0.9 T_g for 2 h have also been measured to characterize the glass densification. A significant deformation recovery zone is observed in the glass after annealing. The shrinkage of the Vickers indents induced by heat treatment has been quantified by determining L_{SR} (Fig. 6b). We find no significant change in L_{SR} with increasing heat treatment time, which is around 35%. Liu et al. have reported that two factors can affect the indentation deformation through densification in such glasses: changes in the coordination numbers of B and Al as a result

Table 3
Crystal content, average crystal size, Vickers hardness at 3 N (H_V), crack initiation resistance (CR), and fracture toughness (K_{Ic}) measured using both indentation and SEPB techniques of as-prepared and heat-treated samples.

Sample ID	Crystal content [wt.%]	Crystal Average Size [nm]	H_V [GPa]	CR [N]	K_{Ic}^{IFT} [MPa·m$^{0.5}$]	K_{Ic}^{SEPB} [MPa·m$^{0.5}$]
BN0	0	-	5.2 ± 0.1	5.1 ± 0.1	0.77 ± 0.01	0.83 ± 0.01
BN4	0	-	5.1 ± 0.1	5.6 ± 0.2	0.77 ±0.01	0.89 ± 0.02
BN8	< 1	15	5.2 ± 0.1	6.3 ± 0.4	0.77 ± 0.02	0.93 ± 0.01
BN12	5 ± 1	30	5.2 ± 0.1	9.1 ± 0.4	0.81 ± 0.01	1.03 ± 0.02
BN16	10 ± 1	50	5.1 ± 0.1	7.9 ± 0.3	0.90 ± 0.02	1.17 ± 0.02

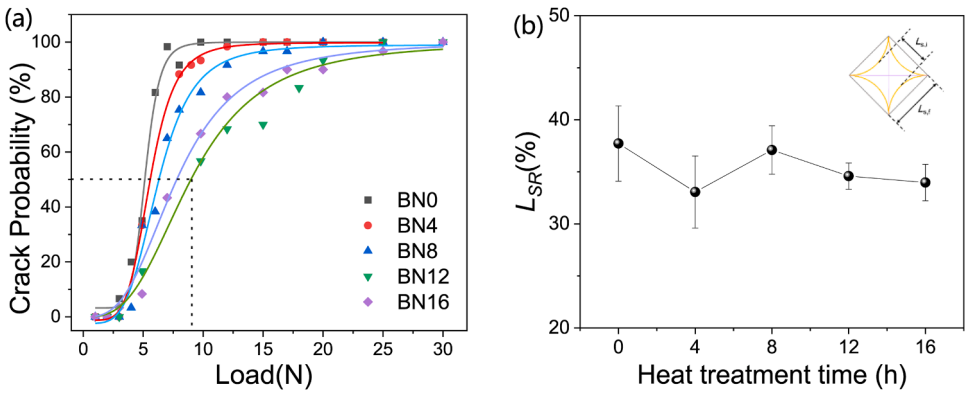

Fig. 6. (a) Crack probability as a function of applied indentation load for the as-prepared glass and heat-treated glass-ceramics, (b) The indentation side recovery (L_{SR}) for the as-prepared glass and heat-treated glass-ceramics.

of the stresses created during indentation, which can lead to more densification; and more open glass networks generally tend to favor more densification [30]. Hence, the stable L_{SR} value implies that a change in the residual glass deformation mechanism is not the main cause of the increase in *CR* after heat treatment.

Furthermore, in oxide glasses with adaptive networks, the energy dissipation caused by the transformation of low-coordinated structural units (such as [BO_3] or [AlO_4]) to higher-coordinated units under applied stress may also lead to higher *CR* [3,60]. The present NMR results show that N_4 decreases from 12.1% for the precursor glass to 10.4% for the BN16 sample, i.e., a decrease in the coordination number of B in the glass-ceramics. The NMR results also show that the average coordination number of Al only decreases very slightly from 4.29 for the precursor glass to 4.26 for the BN16 sample. Both of these changes are beneficial to improve *CR*. Januchta et al. have previously investigated the relationship between the change in coordination number of B and Al and the crack resistance ina lithium aluminoborate glass. They found that when N_4 increased from 16.6% to 29.7% and the CN of Al increased from 4.29 to 4.85 upon compression, a decrease in *CR* from 30 N to 5 N was observed [3]. Frederiksen et al. also reported that for a barium aluminoborate glass, an increase in N_4 from 16% to 22% and in the CN of Al from 4.09 to 4.37 upon compression resulted in a decrease in *CR* from 1 kgf to <0.5 kgf [23]. Compared to these previous studies, the changes in Al and B CNs in this work are relatively small, but the trend of decreasing CNs resulting in higher *CR* is consistent. However, the influence of the crystals on *CR* should also be considered. High residual stresses can be introduced into glass-ceramics due to the mismatch of the coefficient of thermal expansion between the glass matrix and crystals, and these residual stresses may act as the driving force for crack generation. The CTE of the precursor glass is here found to be around 9.8×10^{-6} °C^{-1} (Supporting Fig. S4), while the CTE of $BaNb_2O_6$ crystal has previously been found to be around 11.9×10^{-6} °C^{-1} [61]. That is, the CTE of glass matrix and crystal are relatively similar, and the residual stress induced by the mismatch of CTE is therefore low, which should not promote crack initiation significantly. However, some previous papers have reported that as the crystal content and crystal size increase, the internal residual stress in the glass matrix increases [62]. Sun et al. have reported that the *CR* decreased from 0.68 N of the glass to 0.23 N of heat-treated glass-ceramic as the crystallinity and crystal size increased [63]. As a result, due to the largest crystal content and crystal size in the BN16 sample, the internal residual stress due to CTE mismatch should be the largest in BN16, which likely causes it not to have the highest *CR*.

Next, we consider the influence of the incorporation of the piezoelectric $BaNb_2O_6$ crystal as a secondary phase in the glass matrix on the crack resistance a. It has been reported that part of the applied mechanical energy (related to the induced mechanical stress) can be converted into electrical energy in piezoelectric materials through a phase transformation, or domain wall motion [19,64], which can thus lead to energy dissipation and be beneficial for improving crack resistance. As such, while the internal residual stress caused by CTE mismatch tends to lower *CR*, the observed increase in *CR* upon crystallization is likely due to the combined effect of precipitating a piezoelectric crystal ($BaNb_2O_6$) and decreasing the coordination numbers of Al and B in the glass matrix phase.

To investigate the effect of heat-treatment on fracture toughness, we have used both indentation and SEPB methods (see Fig. 7a-c). The crack lengths *c* and half diagonal lengths *a* upon indentation with 100° pyramidal diamond tip can be measured, as shown in Fig. 7a, and then Eq. (1) can be used to evaluate K_{Ic}^{IFT}. For SEPB measurement, the pre-cracked specimen is subjected to three-point bending to undergo fracture and the peak load value (P_{max}) can be obtained from the load-displacement curve (Fig. 7b) and the measured pre-crack size (Fig. 7c). The determined values of fracture toughness are summarized in Table 3 and Fig. 7d. The indentation fracture toughness of the as-prepared glass BN0 is around 0.77 MPa·$m^{0.5}$, which increases to 0.90 MPa·$m^{0.5}$ for the BN16 sample. The fracture toughness determined from the self-consistent SEPB method of the BN0 sample is 0.83 MPa·$m^{0.5}$, which then increases to 1.17 MPa·$m^{0.5}$ for the BN16 sample. As such, the fracture toughness determined using both test methods thus increase with increasing sample crystallinity.

In addition, the crack path affected by crystals has been characterized. Fig. 8a-c show the morphology of indent impression and tortuosity of the crack path in the BN16 sample without etching before the SEM imaging. The crack in zone 1 exhibits a jagged path and the crack shows relatively high tortuosity along the crystal (white dot) around the crack tip (zone 2). Therefore, the formed crystals in the glass matrix may affect fracture toughness by influencing the path of the propagating crack.

There are many factors that affect the increase in fracture toughness after glass crystallization. Firstly, piezoelectric materials give an electrical response (in the form of a group of dipoles i.e., domains) due to the application of mechanical loading. In addition to the verification of the piezoelectric behavior of the $BaNb_2O_6$ phase done in this work based on the DFPT simulations, previous work has also suggested that it is a ferroelectric phase [65,66]. This can enable that part of the mechanical energy related to the fracture can be converted into electrical energy due to the change in domain direction, which is called domain switching [19,64]. Domain switching is the ability of a ferroelectric material to change the direction of polarization due to the application of a mechanical stress. That is, the application of mechanical loading can result in domain switching, which also dissipates some energy. Hence, during crack propagation in materials with piezoelectric secondary phase, a part of the mechanical energy can be converted into electrical energy, so crack propagation energy decreases further, enhancing the fracture toughness [19]. Indeed, nanoscale piezoelectric structures (as those in the present samples) can show much larger effects compared to macroscopic materials [67]. According to the literature, the

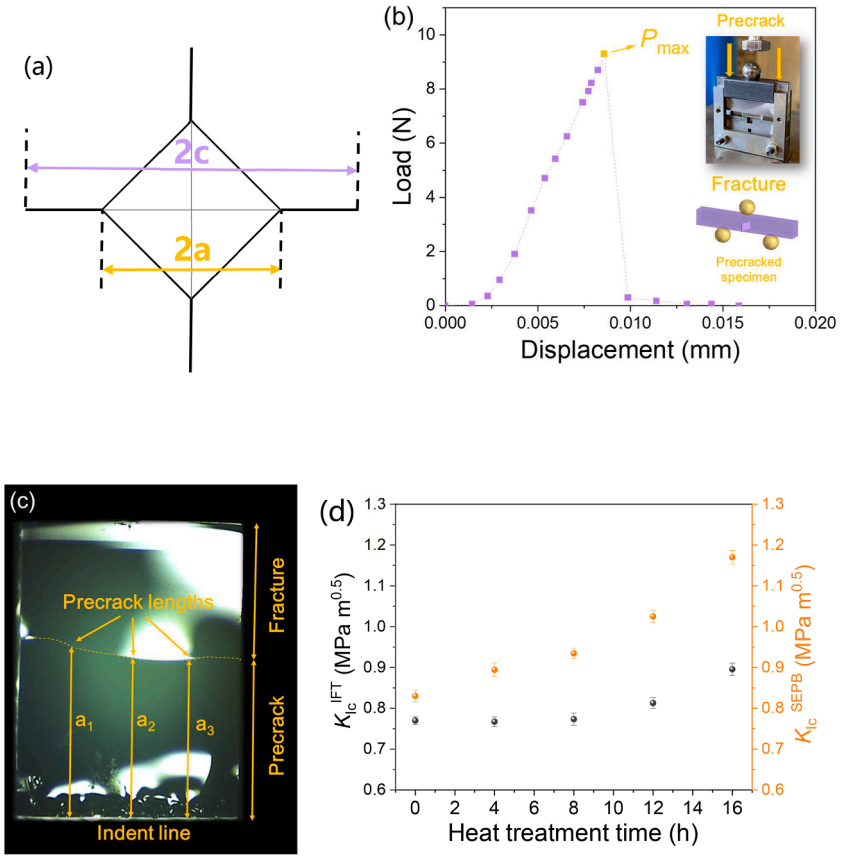

Fig. 7. Fracture toughness measurement: (a) The measurement of indentation fracture toughness. (b) Load-displacement curve of three-point bending of the pre-cracked SEPB specimen. The inset shows the bridge-compression fixture (pre-crack) and the three-point bending fixture with a pre-cracked specimen (fracture). (c) Post-fractured SEPB specimen. (d) Fracture toughness (K_{Ic}) for all samples.

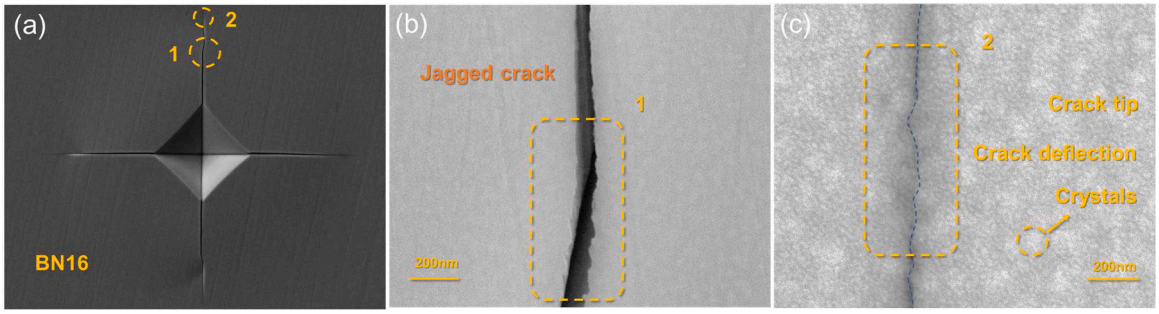

Fig. 8. SEM images showing the morphology of indent impression in the BN16 sample without etching. (a) Morphology of indent impression, (b) crack path in zone 1, and (c) crack path in zone 2.

piezoelectric phenomenon can also change the mode of stress that acts on the crack tip, arresting the crack propagation [68–70]. The schematic diagram of a possible crack propagation path in glass-ceramic with piezoelectric secondary phases is shown in Supporting Fig. S5. Therefore, the formation of the $BaNb_2O_6$ phase in the glass-ceramics appears to enhance the fracture toughness by domain switching and/or energy dissipation [65]. However, understanding the detailed mechanism requires additional investigation.

Secondly, from the point of view of the crystals in the glass-ceramics (independent of their piezoelectric features), heterogeneous microstructure can generally improve fracture toughness by effectively dissipating the high local stresses through crack deflection, multiple cracking, crack bridging, and crack branching operated at the crack tip [71,72]. Such crack deflection caused by crystals has been confirmed by SEM imaging (Fig. 8c) in the present samples. In previous work, Peitl et al. reported that the K_{Ic} increased from 0.7 MPa·m$^{0.5}$ for glass to 0.9 MPa·m$^{0.5}$ for glass-ceramic containing a 40% crystal fraction [10]. In this work, according to the phase microstructure analysis, the crystal content increases to 10% and the crystal size increases to 50 nm in the BN16 sample, with a corresponding increase in K_{Ic}^{SEPB} from 0.83 MPa·m$^{0.5}$ to 1.17 MPa·m$^{0.5}$. In comparison, the change in crystallinity in this work is relatively small, suggesting that the toughening effect due to the crystalline microstructure (causing crack deflection etc.) is not the only reason for the increase in fracture toughness of the present glass-ceramics. This again appears to point to the important role of the piezoelectric crystal phase.

Lastly, from the point of view of the glass matrix structure, To et al. found that bond switching events mainly occur near the crack tips and crack propagation path in oxide glass with boron and aluminum, which could be a way to improve the fracture toughness [1]. That is, a higher

K_{Ic} was observed due to the increased average CN upon compression. According to the present NMR results and the previous discussion, we find that the coordination numbers of both B and Al become lower after heat treatment. This effect should therefore counteract the positive effect of the crystals on K_{Ic}. However, as discussed previously, the CN changes upon heat treatment are relatively small, i.e., the toughening effect of the crystals plays the dominant role compared to the change in the glass matrix phase.

Crack resistance (i.e., resistance to crack initiation) and fracture toughness (i.e., resistance to crack growth) are both important parameters for evaluating the glass/glass-ceramics mechanical performance. Although there is no systematic relation between *CR* and K_{Ic} [18], it is challenging to improve *CR* and K_{Ic} simultaneously, since crystal formation can lead to residual stresses that may lead to crack initiation [10], while crack deflection, pinning or bridging caused by the presence of crystals are beneficial to improve the fracture toughness [7]. Furthermore, considering the low crystallinity in most transparent glass-ceramics, the influence of the glass matrix on the mechanical properties should also be considered. Through the design of glass composition and adjustment of heat treatment parameters, the piezoelectric secondary phase $BaNb_2O_6$ has here been induced in the aluminoborate glass, achieving the simultaneous improvement of crack resistance and fracture toughness, as well as maintaining a certain level of transparency, which provides a new approach to addressing the problem of glass brittleness.

4. Conclusion

In this work we have studied the changes in structure and mechanical properties upon heat treatment of a Nb_2O_5-doped barium aluminoborate glass. Importantly, we have found that both crack initiation resistance and fracture toughness are significantly improved after heat treatment, and even the most crystallized glass-ceramics retain significant transmittance. *CR* increases from 5.1 N of the as-prepared glass to 9.1 N of BN12, an increase of 78%. At the same time, the K_{Ic}^{SEPB} increases from 0.83 MPa·$m^{0.5}$ of as-prepared glass to 1.17 MPa·$m^{0.5}$ of BN16, an increase of 41%. Based on Raman and NMR spectroscopy analyses, the coordination numbers of boron and aluminum decrease in the glass matrix upon heat treatment, which is beneficial to energy dissipation under mechanical stress to improve *CR*. Furthermore, the piezoelectric phase $BaNb_2O_6$ formed in the glass-ceramics is suggested as a factor for improving *CR* by energy conversion (mechanical energy to electric energy) and/or domain switching, although the exact mechanism requires additional investigation. The increasing crystallinity and crystal size are also beneficial to increase the fracture toughness of the glass-ceramics. The present discovery thus addresses the difficult problem of simultaneously improving damage resistance and damage tolerance in glass-ceramics, which will facilitate the future design of transparent glass-ceramics.

CRediT authorship contribution statement

Qi Zhang: Conceptualization, Investigation, Formal analysis, Writing – original draft. **Daming Sun:** Investigation, Writing – review & editing. **Tao Du:** Investigation, Formal analysis, Writing – review & editing. **Lars R. Jensen:** Investigation, Writing – review & editing. **Deyong Wang:** Investigation, Writing – review & editing. **Vladimir Popok:** Investigation, Writing – review & editing. **Randall E. Youngman:** Investigation, Formal analysis, Writing – review & editing. **Morten M. Smedskjaer:** Conceptualization, Supervision, Writing – original draft.

Declaration of Competing Interest

The authors declare that they have no known competing financial interests or personal relationships that could have appeared to influence the work reported in this paper.

Data availability

Data will be made available on request.

Acknowledgments

This work was supported by the European Union's Horizon 2020 research and innovation programme under the Marie Sklodowska-Curie (882520, 101018156) and China Scholarship Council (202107000016).

Supplementary materials

Supplementary material associated with this article can be found, in the online version, at doi:10.1016/j.apmt.2023.101888.

References

[1] T. To, S.S. Sørensen, J.F. Christensen, R. Christensen, L.R. Jensen, M. Bockowski, M. Bauchy, M.M. Smedskjaer, Bond switching in densified oxide glass enables record-high fracture toughness, ACS Appl. Mater. Interfaces 13 (2021) 17753–17765.
[2] J.C. Mauro, A. Tandia, K.D. Vargheese, Y.Z. Mauro, M.M. Smedskjaer, Accelerating the design of functional glasses through modeling, Chem. Mater. 28 (2016) 4267–4277.
[3] K. Januchta, R.E. Youngman, A. Goel, M. Bauchy, S.L. Logunov, S.J. Rzoska, M. Bockowski, L.R. Jensen, M.M. Smedskjaer, Discovery of ultra-crack-resistant oxide glasses with adaptive networks, Chem. Mater. 29 (2017) 5865–5876.
[4] G.D. Quinn, J.J. Swab, Fracture toughness of glasses as measured by the SCF and SEPB methods, J. Eur. Ceram. Soc. 37 (2017) 4243–4257.
[5] M.B. Østergaard, S.R. Hansen, K. Januchta, T. To, S.J. Rzoska, M. Bockowski, M. Bauchy, M.M. Smedskjaer, Revisiting the dependence of poisson's ratio on liquid fragility and atomic packing density in oxide glasses, Materials 12 (2019) 2439.
[6] X. Ke, Z. Shan, Z. Li, Y. Tao, Y. Yue, H. Tao, Toward hard and highly crack resistant magnesium aluminosilicate glasses and transparent glass-ceramics, J. Am. Ceram. Soc. 103 (2020) 3600–3609.
[7] Q. Fu, G.H. Beall, C.M. Smith, Nature-inspired design of strong, tough glass-ceramics, MRS Bull. 42 (2017) 220–225.
[8] C. Gonzalez-Oliver, P. James, Crystal nucleation and growth in a Na_2O–2CaO–$3SiO_2$ glass, J. NonCryst. Solids 38 (1980) 699–704.
[9] B. Deng, J. Luo, J.T. Harris, C.M. Smith, M.E. McKenzie, Molecular dynamics simulations on fracture toughness of Al_2O_3–SiO_2 glass-ceramics, Scr. Mater. 162 (2019) 277–280.
[10] O. Peitl, E.D. Zanotto, F.C. Serbena, L.L. Hench, Compositional and microstructural design of highly bioactive P_2O_5–Na_2O–CaO–SiO_2 glass-ceramics, Acta Biomater. 8 (2012) 321–332.
[11] J. Quinn, V. Sundar, I.K. Lloyd, Influence of microstructure and chemistry on the fracture toughness of dental ceramics, Dent. Mater. 19 (2003) 603–611.
[12] G.H. Beall, Chain silicate glass-ceramics, J. NonCryst. Solids 129 (1991) 163–173.
[13] Q. Fu, E.M. Aaldenberg, E.N. Coon, T.M. Gross, A.M. Whittier, B.M. Abel, D. E. Baker, Tough, bioinspired transparent glass-ceramics, Adv. Eng. Mater. (2022), 2200350.
[14] L. Martel, M. Allix, F. Millot, V. Sarou-Kanian, E. Véron, S. Ory, D. Massiot, M. Deschamps, Controlling the size of nanodomains in calcium aluminosilicate glasses, J. Phys. Chem. C 115 (2011) 18935–18945.
[15] Z. Li, C. Chen, W. Shen, D. Zhou, L.R. Jensen, X. Qiao, J. Ren, J. Du, Y. Zhang, J. Qiu, The transformation from translucent into transparent rare earth ions doped oxyfluoride glass-ceramics with enhanced luminescence, Adv. Opt. Mater. (2022), 2102713.
[16] D. Chen, H. Miyoshi, H. Masui, T. Akai, T. Yazawa, NMR study of structural changes of alkali borosilicate glasses with heat treatment, J. NonCryst. Solids 345 (2004) 104–107.
[17] T. Furukawa, W.B. White, Raman spectroscopy of heat-treated B2O3-SiO2 glasses, J. Am. Ceram. Soc. 64 (1981) 443–447.
[18] T. To, L.R. Jensen, M.M. Smedskjaer, On the relation between fracture toughness and crack resistance in oxide glasses, J. NonCryst. Solids 534 (2020), 119946.
[19] A.S. Verma, D. Kumar, A.K. Dubey, A review of an innovative concept to increase the toughness of the ceramics by piezoelectric secondary phases, Ceram. Int. 44 (2018) 16119–16127.
[20] Q. Zhang, X. Du, S. Tan, D. Tang, K. Chen, T. Zhang, Effect of Nb_2O_5 doping on improving the thermo-mechanical stability of sealing interfaces for solid oxide fuel cells, Sci. Rep. 7 (2017) 1–8.
[21] Z. Dong, J. Lai, W. Huang, S. Pang, H. Zhuang, H. Zhan, D. Tang, K. Chen, T. Zhang, A robust glass-ceramic sealing material for solid oxide fuel cells: effect of $Ba_3Nb_{10}O_{28}$ phase, J. Eur. Ceram. Soc. 39 (2019) 1540–1545.

[22] L.S.A. Gallo, F. Célarié, J. Bettini, A.C.M. Rodrigues, T. Rouxel, E.D. Zanotto, Fracture toughness and hardness of transparent MgO–Al2O3–SiO2 glass-ceramics, Ceram. Int. 48 (2022) 9906–9917.

[23] K.F. Frederiksen, K. Januchta, N. Mascaraque, R.E. Youngman, M. Bauchy, S. J. Rzoska, M. Bockowski, M.M. Smedskjaer, Structural compromise between high hardness and crack resistance in aluminoborate glasses, J. Phys. Chem. B 122 (2018) 6287–6295.

[24] S. Liu, J. Wang, J. Ding, H. Hao, L. Zhao, S. Xia, Crystallization, microstructure and dielectric properties of the SrO-BaO-Nb2O5-Al2O3-SiO2 based glass ceramics added with ZrO2, Ceram. Int. 45 (2019) 4003–4008.

[25] A. Mazzoli, O. Favoni, Particle size, size distribution and morphological evaluation of airborne dust particles of diverse woods by Scanning Electron Microscopy and image processing program, Powder Technol. 225 (2012) 65–71.

[26] K. Kapat, P.K. Srivas, A.P. Rameshbabu, P.P. Maity, S. Jana, J. Dutta, P. Majumdar, D. Chakrabarti, S. Dhara, Influence of porosity and pore-size distribution in Ti6Al4 V foam on physicomechanical properties, osteogenesis, and quantitative validation of bone ingrowth by micro-computed tomography, ACS Appl. Mater. Interfaces 9 (2017) 39235–39248.

[27] D. Massiot, F. Fayon, M. Capron, I. King, S.Le Calvé, B. Alonso, J.O. Durand, B. Bujoli, Z. Gan, G. Hoatson, Modelling one-and two-dimensional solid-state NMR spectra, Magn. Reson. Chem. 40 (2002) 70–76.

[28] R.K. Harris, E.D. Becker, S.M. Cabral De Menezes, P. Granger, R.E. Hoffman, K. W. Zilm, Further conventions for NMR shielding and chemical shifts (IUPAC Recommendations 2008), Pure Appl. Chem. 80 (2008) 59–84.

[29] E. Papulovskiy, D.F. Khabibulin, V.V. Terskikh, E.A. Paukshtis, V.M. Bondareva, A. A. Shubin, A.S. Andreev, O. Lapina, Effect of impregnation on the structure of niobium oxide/alumina catalysts studied by multinuclear Solid-State NMR, FTIR, and quantum chemical calculations, J. Phys. Chem. C 119 (2015) 10400–10411.

[30] P. Liu, K. Januchta, L.R. Jensen, M. Bauchy, M.M. Smedskjaer, Competitive effects of free volume, rigidity, and self-adaptivity on indentation response of silicoaluminoborate glasses, J. Am. Ceram. Soc. 103 (2020) 944–954.

[31] M. Wada, H. Furukawa, K. Fujita, Crack resistance of glass on Vickers indentation, in: Proc. Int. Congr. Glass, 1974, pp. 39–46.

[32] S. Yoshida, J.-C. Sanglebœuf, T. Rouxel, Quantitative evaluation of indentation-induced densification in glass, J. Mater. Res. 20 (2005) 3404–3412.

[33] K. Januchta, R.E. Youngman, L.R. Jensen, M.M. Smedskjaer, Mechanical property optimization of a zinc borate glass by lanthanum doping, J. NonCryst. Solids 520 (2019), 119461.

[34] T.M. Gross, H. Liu, Y. Zhai, L. Huang, J. Wu, The impact of densification on indentation fracture toughness measurements, J. Am. Ceram. Soc. 103 (2020) 3920–3929.

[35] G. Anstis, P. Chantikul, B.R. Lawn, D. Marshall, A critical evaluation of indentation techniques for measuring fracture toughness: I, direct crack measurements, J. Am. Ceram. Soc. 64 (1981) 533–538.

[36] X. Ren, T. Du, H. Peng, L.R. Jensen, C.A. Biscio, L. Fajstrup, M. Bauchy, M. M. Smedskjaer, Irradiation-induced toughening of calcium aluminoborosilicate glasses, Mater. Today Commun. 31 (2022), 103649.

[37] T. To, F. Célarié, C. Roux-Langlois, A. Bazin, Y. Gueguen, H. Orain, M.Le Fur, V. Burgaud, T. Rouxel, Fracture toughness, fracture energy and slow crack growth of glass as investigated by the Single-Edge Precracked Beam (SEPB) and Chevron-Notched Beam (CNB) methods, Acta Mater. 146 (2018) 1–11.

[38] T. To, S.S. Sørensen, M. Stepniewska, A. Qiao, L.R. Jensen, M. Bauchy, Y. Yue, M. M. Smedskjaer, Fracture toughness of a metal–organic framework glass, Nat. Commun. 11 (2020) 1–9.

[39] G. Kresse, J. Furthmüller, Efficient iterative schemes for ab initio total-energy calculations using a plane-wave basis set, Phys. Rev. B 54 (1996) 11169.

[40] G. Kresse, J. Hafner, Ab initio molecular dynamics for liquid metals, Phys. Rev. B 47 (1993) 558.

[41] J.P. Perdew, K. Burke, M. Ernzerhof, Generalized gradient approximation made simple, Phys. Rev. Lett. 77 (1996) 3865.

[42] H. Li, L. Wang, L. Xu, A. Li, P. Mao, Q. Wu, Z. Xie, First-principles study on the structural, elastic, piezoelectric and electronic properties of (BaTiO3, LiTaO3)-modified KNbO3, Mater. Today Commun. 26 (2021), 102092.

[43] F. Wang, Z. Dai, Y. Gu, X. Cheng, Y. Jiang, F. Ouyang, J. Xu, X. Xu, First-principles analysis of a molecular piezoelectric meta-nitroaniline, RSC Adv. 8 (2018) 16991–16996.

[44] K. Choudhary, K.F. Garrity, V. Sharma, A.J. Biacchi, A.R. Hight Walker, F. Tavazza, High-throughput density functional perturbation theory and machine learning predictions of infrared, piezoelectric, and dielectric responses, npj Comput. Mater. 6 (2020) 64.

[45] T. Edwards, T. Endo, J.H. Walton, S. Sen, Observation of the transition state for pressure-induced $BO_3 \rightarrow BO_4$ conversion in glass, Science 345 (2014) 1027–1029.

[46] L.M. Marcondes, H. Bradtmüller, S.N.C. dos Santos, L.K. Nolasco, C.R. Mendonça, S.H. Santagneli, G.Y. Poirier, M. Nalin, Structural and luminescence characterization of europium-doped niobium germanate glasses and glass-ceramics: novel insights from ^{93}Nb solid-state NMR spectroscopy, Ceram. Int. (2022).

[47] O.B. Lapina, D.F. Khabibulin, K.V. Romanenko, Z. Gan, M.G. Zuev, V. N. Krasil'nikov, V.E. Fedorov, ^{93}Nb NMR chemical shift scale for niobia systems, Solid State Nucl. Magn. Reson. 28 (2005) 204–224.

[48] A. Flambard, J.-J. Videau, L. Delevoye, T. Cardinal, C. Labrugère, C. Rivero, M. Couzi, L. Montagne, Structure and nonlinear optical properties of sodium–niobium phosphate glasses, J. NonCryst. Solids 354 (2008) 3540–3547.

[49] S. Hsu, J. Wu, S. Yung, T. Chin, T. Zhang, Y. Lee, C. Chu, J. Ding, Evaluation of chemical durability, thermal properties and structure characteristics of Nb–Sr-phosphate glasses by Raman and NMR spectroscopy, J. NonCryst. Solids 358 (2012) 14–19.

[50] H. Maeda, S. Lee, T. Miyajima, A. Obata, K. Ueda, T. Narushima, T. Kasuga, Structure and physicochemical properties of $CaO–P_2O_5–Nb_2O_5–Na_2O$ glasses, J. NonCryst. Solids 432 (2016) 60–64.

[51] E. De Araujo, J. De Paiva, J. Freitas Jr, A. Sombra, Raman and infrared spectroscopy studies of $LiNbO_3$ in niobate glass-ceramics, J. Phys. Chem. Solids 59 (1998) 689–694.

[52] T. Cardinal, E. Fargin, G.Le Flem, S. Leboiteux, Correlations between structural properties of $Nb_2O_5–NaPO_3–Na_2B_4O_7$ glasses and non-linear optical activities, J. NonCryst. Solids 222 (1997) 228–234.

[53] K.S. Rao, K.H. Yoon, Review of electrooptic and ferroelectric properties of barium sodium niobate single crystals, J. Mater. Sci. 38 (2003) 391–400.

[54] J. Carruthers, M. Grasso, Phase equilibria relations in the ternary system $BaO–SrO–Nb_2O_5$, J. Electrochem. Soc. 117 (1970) 1426.

[55] H. Li, Y. Su, L. Li, D.M. Strachan, Raman spectroscopic study of gadolinium (III) in sodium-aluminoborosilicate glasses, J. NonCryst. Solids 292 (2001) 167–176.

[56] Q. Zhang, K. Chen, D. Tang, T. Zhang, Effects of Nb_2O_5 and Gd_2O_3 doping on boron volatility and activity between glass seals and lanthanum-containing cathode, J. Eur. Ceram. Soc. 37 (2017) 1547–1555.

[57] S. Morimoto, Phase separation and crystallization in the system $SiO_2–Al_2O_3–P_2O_5–B_2O_3–Na_2O$ glasses, J. NonCryst. Solids 352 (2006) 756–760.

[58] M. Abdel-Baki, F. Abdel-Wahab, A. Radi, F. El-Diasty, Factors affecting optical dispersion in borate glass systems, J. Phys. Chem. Solids 68 (2007) 1457–1470.

[59] K. Januchta, P. Liu, S.R. Hansen, T. To, M.M. Smedskjaer, Indentation cracking and deformation mechanism of sodium aluminoborosilicate glasses, J. Am. Ceram. Soc. 103 (2020) 1656–1665.

[60] G.A. Rosales-Sosa, A. Masuno, Y. Higo, H. Inoue, Crack-resistant $Al_2O_3–SiO_2$ glasses, Sci. Rep. 6 (2016) 1–7.

[61] A. Lashtabeg, Niobium Based Materials for Use as Current Collectors in the Anode of Solid Oxide Fuel Cells (Ph.D thesis), University of St Andrews, 2004.

[62] F.C. Serbena, E.D. Zanotto, Internal residual stresses in glass-ceramics: a review, J. NonCryst. Solids 358 (2012) 975–984.

[63] D. Sun, Q. Zhang, P. Liu, L.R. Jensen, D. Wang, M.M. Smedskjaer, Balancing fracture toughness and transparency in barium titanosilicate glass-ceramics, Ceram. Int. 49 (2023) 17479–17487.

[64] X.M. Chen, X.Q. Liu, F. Liu, X.B. Zhang, 3Y-TZP ceramics toughened by $Sr_2Nb_2O_7$ secondary phase, J. Eur. Ceram. Soc. 21 (2001) 477–481.

[65] S. Dhage, R. Pasricha, V. Ravi, Preparation of ferroelectric BaNb2O6 by the urea method, Mater. Lett. 59 (2005) 1929–1931.

[66] C. Dudhe, S. Nagdeote, R. Atram, Investigation of polymorphic tetragonal phase in BaNb2O6 nanoparticles by ferroelectricity, Mater. Lett. 176 (2016) 202–204.

[67] V.N. Popok, M. Chirumamilla, T. Krekeler, M. Ritter, K. Pedersen, Magnetron sputter grown AlN nanostructures with giant piezoelectric response toward energy generation, ACS Appl. Nano Mater. (2023).

[68] R. Rajapakse, X. Zeng, Toughening of conducting cracks due to domain switching, Acta Mater. 49 (2001) 877–885.

[69] C.C. Fulton, H. Gao, Effect of local polarization switching on piezoelectric fracture, J. Mech. Phys. Solids 49 (2001) 927–952.

[70] W. Yang, F. Fang, M. Tao, Critical role of domain switching on the fracture toughness of poled ferroelectrics, Int. J. Solids Struct. 38 (2001) 2203–2211.

[71] K. Maeda, K. Iwasaki, S. Urata, K. Akatsuka, A. Yasumori, 3D microstructure and crack pathways of toughened $CaO–Al_2O_3–SiO_2$ glass by precipitation of hexagonal $CaAl_2Si_2O_8$ crystal, J. Am. Ceram. Soc. 102 (2019) 5535–5544.

[72] M. Chen, S. Zhu, M. Shen, F. Wang, Y. Niu, Effect of NiCrAlY platelets inclusion on the mechanical and thermal shock properties of glass matrix composites, Mater. Sci. Eng. A Struct. Mater. 528 (2011) 1360–1366.